



Insights into the role of active site density in the fuel cell performance of Co-N-C catalysts



Linyun Chen^a, Xiaofang Liu^a, Lirong Zheng^b, Yongcheng Li^a, Xu Guo^a, Xin Wan^a, Qingtao Liu^a, Jiaxiang Shang^a, Jianglan Shui^{a,*}

^a School of Materials Science and Engineering, Beihang University, No. 37 Xueyuan Road, Beijing 100083, China

^b Beijing Synchrotron Radiation Facility, Institute of High Energy Physics, Chinese Academy of Sciences, No. 19 Yuquan Road, Beijing 100049, China

ARTICLE INFO

Keywords:

Single-atom catalyst
Co-N-C
Active site
Fuel cell
Power density

ABSTRACT

Improvement of proton exchange membrane fuel cell (PEMFC) performance of Co-N-C electrocatalyst requires an in-depth understanding of performance enhancement mechanism. Herein, we synthesize a series of Co-N-C catalysts with different CoN_4 densities. CoN_4 active sites (electrochemically accessible ones) and CoN_4 species are differentiated in the study. The power density shows a slow linear increase in the low concentration region and an accelerated increase in the high concentration region of CoN_4 active sites, showing the crucial role of the high active site density to the high power density of Co-N-C. The optimized Co-N-C achieves a high power density of 826 mW cm^{-2} . Meanwhile, CoN_4 ORR turnover frequency (TOF) is calculated to be 0.01 s^{-1} at 0.8 V vs. RHE in acid media. The results allow us to predict that many non-precious metal catalysts with only moderate activity may have considerable PEMFC performance as long as possessing sufficiently dense active sites.

1. Introduction

Proton exchange membrane fuel cells (PEMFCs) capable of efficiently converting hydrogen energy into electricity have attracted worldwide attention [1–3]. Its bottleneck reaction is the oxygen reduction reaction (ORR), which currently relies on Pt-based catalysts [3–5]. Unfortunately, the scarcity and high cost of Pt limit the large-scale application of PEMFCs. Therefore, it is necessary to develop low-cost, efficient and durable non-precious metal catalysts (NPMCs) to replace Pt catalysts [6–9]. Among various NPMCs, M-N-C ($M = \text{Fe}, \text{Co}$) catalysts represent attractive types, which have nitrogen-coordinated transition metal atoms FeN_x or CoN_x as the active sites [10–19]. So far, Fe-N-C catalysts have achieved high fuel cell power densities of $800\text{--}1100 \text{ mW cm}^{-2}$ [20–27], however, they generally suffer from a fast performance decay in PEMFCs [20,28–30]. The possible reasons could be attributed to (1) leaching of the metal site, (2) oxidative attack by H_2O_2 , (3) protonation of the active sites, (4) micropore flooding and (5) surface oxidation of carbon [28–32].

Compared with Fe-N-C catalysts, Co-N-C catalysts are particularly attractive in terms of higher PEMFC stability due to its immunity to Fenton's reaction [33–36]. Although the power density of Co-N-C fuel cell is still relatively lower than that of Fe-N-C fuel cells, it has gained a rapid boost recently, which arouses interest in the in-depth study of Co-

N-C catalysts. Wang et al. has announced a volcano relationship of ORR activity (measured by RDE) vs. Co content in Co-N-C catalysts [34,36]. It is reasonable that an enhancement of Co content (before Co agglomeration) increases the number of CoN_x moieties, thus leading to the improved ORR activity. Naturally, we can predict that high-density CoN_x moieties would produce a high PEMFC performance. However, it should be clarified that not all CoN_x moieties can be referred to "active sites" to contribute ORR activity. Only the CoN_x moieties distributed on the catalyst surface may participate in ORR, while the rest deep inside the dense carbon may stay inactive. Therefore, the number of active sites rather than the total Co content determines the fuel cell performance [13]. Nevertheless, the correlation of CoN_x active site density and fuel cell power density is still unclear for Co-N-C catalysts. Moreover, the crucial parameter, i.e. ORR turnover frequency (TOF) on an active CoN_4 site, has not been investigated yet in the acidic electrolyte. To precisely investigate the active sites in Co-N-C catalysts, an ideal research carrier i.e. Co-N-C single-atom catalysts (SACs) is highly desirable, in which all the Co elements are in the state of atomic CoN_x moiety [35,37–39].

Herein, a series of Co-N-C SACs with different densities of CoN_4 active sites are synthesized for a quantitative study on the structure-property relationship. The density of electrochemically accessible CoN_4 active sites is measured for all Co-N-C SACs. The ORR TOF on a single

* Corresponding author.

E-mail address: shuijianglan@buaa.edu.cn (J. Shui).

active CoN_4 site is for the first time calculated to be 0.01 s^{-1} at 0.8 V (vs. RHE) in acidic media. The PEMFC power density increases slowly and linearly with the CoN_4 active site density in the low density region ($18.9\text{--}30.3 \mu\text{mol}_{\text{site}} \text{ g}^{-1}$); whereas it shows an accelerated increase trend in the high density region (above $30.3 \mu\text{mol}_{\text{site}} \text{ g}^{-1}$). The optimized Co-N-C SAC with dense active sites achieves remarkable PEMFC power densities among the top performance of Co-N-C catalysts. In addition, density functional theory (DFT) calculations together with peroxide reduction reaction (PRR) experiments clarify a direct $4e^-$ pathway instead of a $2e^- + 2e^-$ pathway for ORR on a CoN_4 site, which accounts for the relatively higher stability of Co-N-C than Fe-N-C in PEMFCs.

2. Experimental part

2.1. Preparation of catalysts

The Co-N-C catalyst was synthesized according to the reported method [12,20]. Briefly, a mixture of 2-methylimidazole (980 mg, Sigma-Aldrich) and ZnO (410 mg, Sigma-Aldrich) was grinded for 10 min, sealed in an autoclave under Ar atmosphere, and heated at 220°C for 18 h. The obtained white powder (ZIF-8) was mixed with 1, 10-phenanthroline ($\geq 99\%$, Aldrich) and cobalt acetate (CoAc , 95%, Aldrich) in a mixture of ethanol and deionized (DI) water ($18.3 \text{ M}\Omega \text{ cm}$, Millipore) (ethanol/water volume ratio = 1/2) with $\text{CoAc}/\text{phen}/\text{ZIF-8}$ wt ratio = 1.6/18.4/80, and stirred at 60°C for 12 h and then dried at 80°C overnight. The powder was subsequently ball-milled for 3 h under 300 rpm in a 50 cm^3 Teflon jar with agate balls (diameter 5 mm). The weight ratio of powder to balls is 1:20. Finally, the Co-N-C catalyst was obtained by annealing the ball-milled mixture at 1000°C in Ar atmosphere for 180 min with a heating rate of $5^\circ\text{C}/\text{min}$ from room temperature. During the cooling, the tube furnace temperature was kept at 800°C for 8 min and meanwhile the filling gas was switched from Ar to NH_3 at 800°C . The obtained product was denoted as $1.6\%\text{CoNC-ArNH}_3$. The 1.6% represented CoAc weight ratio in the precursor. Other CoNC-ArNH₃ catalysts with different CoAc weight ratio in the precursor were prepared using the same procedure, denoted as $0.4\%\text{CoNC-ArNH}_3$ ($\text{CoAc}/\text{phen}/\text{ZIF} = 0.4/19.6/80$), $0.6\%\text{CoNC-ArNH}_3$ ($\text{CoAc}/\text{phen}/\text{ZIF} = 0.6/19.4/80$), $0.8\%\text{CoNC-ArNH}_3$ ($\text{CoAc}/\text{phen}/\text{ZIF} = 0.8/19.2/80$), $1.0\%\text{CoNC-ArNH}_3$ ($\text{CoAc}/\text{phen}/\text{ZIF} = 1/19/80$), $1.2\%\text{CoNC-ArNH}_3$ ($\text{CoAc}/\text{phen}/\text{ZIF} = 1.2/18.8/80$), $1.4\%\text{CoNC-ArNH}_3$ ($\text{CoAc}/\text{phen}/\text{ZIF} = 1.4/18.6/80$) and $1.8\%\text{CoNC-ArNH}_3$ ($\text{CoAc}/\text{phen}/\text{ZIF} = 1.8/18.2/80$). The comparison sample Fe-N-C catalyst was prepared according to the literature method [20].

2.2. Electrochemical measurements

The oxygen reduction reaction (ORR) activities of catalysts were measured by a rotating ring-disk electrode (RRDE, Pine ResearchInstrumentation, USA) technique with a CHI Electrochemical Station (model 760e) at room temperature. Linear sweep voltammetry (LSV) curves were carried out in O_2 -saturated $0.5 \text{ M H}_2\text{SO}_4$ (or 0.1 M HClO_4 for Pt/C) water solution at a rotating speed of 1600 rpm within a three-electrode cell. A saturated calomel electrode (SCE) and a gold wire were used as reference and counter electrodes, respectively. The measured potentials versus SCE were converted to a reversible hydrogen electrode (RHE) scale according to the Nernst equation ($E_{\text{RHE}} = E_{\text{SCE}} + 0.0591 \text{ pH} + 0.273$). The catalyst ink was prepared by mixing the catalyst with a Nafion ionomer (DuPont) isopropanol/water solution (Catalyst/Nafion weight ratio = 9/1). After sonicating for 30 min, the catalyst ink was loaded onto a glass carbon electrode with a loading of 0.5 mg cm^{-2} . Loading of Pt/C(20%) was $50 \mu\text{g}_{\text{Pt}} \text{ cm}^{-2}$.

KSCN tolerance test was conducted by adding 2 mL KSCN water solution (0.375 M) into O_2 -saturated $150 \text{ mL H}_2\text{SO}_4$ (0.5 M) electrolyte after collecting a normal linear sweep voltammetry (LSV) curve of the catalyst. Subsequently, another LSV curve was measured with the

presence of KSCN in the electrolyte.

The Pt-ring potential was set at 1.3 V vs. RHE to detect the yield of H_2O_2 . The hydrogen peroxide yield ($\text{H}_2\text{O}_2 \%$) and the electron transfer number (n) were calculated using the following equation:

$$\text{H}_2\text{O}_2(\%) = 200 \times \frac{\frac{I_R}{N}}{I_D + \frac{I_R}{N}} \quad (1)$$

$$n = 4 \times \frac{I_D}{I_P + \frac{I_R}{N}} \quad (2)$$

For peroxide reduction reaction (PRR) analysis [40], the PRR polarization curves were recorded with a scan rate of 5 mV s^{-1} at a rotation speed of 1600 rpm in Ar-saturated 0.1 M HClO_4 with $1.3 \text{ mM H}_2\text{O}_2$ or $10 \text{ mM H}_2\text{O}_2$.

For electrochemical stripping experiments [16,41], the catalysts were measured in 0.5 M acetate buffer ($\text{pH } 5.2$) from sodium acetate (99%, Sigma-Aldrich) and glacial acetic acid. After the typical break-in procedure and background scan, we recorded LSV curves of different samples. 1) Record a CV baseline in Ar-saturated electrolyte from -0.3 to 0.25 V vs. RHE, 10 mV s^{-1} (denoted as unpoisoned sample). 2) Dip RDE into 125 mM NaNO_2 solution for 5 min at open circuit potential (OCP), 300 rpm. 3) Wash electrode in DI water for 1 min at OCP, 300 rpm. 4) Wash electrode in electrolyte solution for 5 min at OCP, 300 rpm. 5) Wash electrode in DI water for 1 min at OCP, 300 rpm. 6) Record LSV in O_2 -saturated electrolyte, from 0.3 to 0.85 V vs. RHE, 10 mV s^{-1} (to record poisoned ORR LSV). 7) Record another CV in Ar-saturated electrolyte, from -0.35 to 0.25 V vs. RHE, 10 mV s^{-1} (denoted as poisoned sample).

Q_{strip} is the excess coulometric charge associated with the stripping peak. n_{strip} is the number of electrons associated with the reduction of one adsorbed nitrosyl per CoN_4 site. A transfer of 5 electrons per stripped molecule is used. The gravimetric active site density (MSD), which is the amount of active sites normalized to the mass, is calculated from:

$$\text{MSD(mol sites g}^{-1}\text{)} = \frac{Q_{\text{strip}}(\text{C g}^{-1})}{n_{\text{strip}} F(\text{C mol}^{-1})} \quad (3)$$

The kinetic current (at 0.8 V vs. RHE), i_k is estimated as follows, where i was taken as the current at 0.8 V vs. RHE and i_{lim} was taken as the current achieved at 0.3 V vs. RHE:

$$i_k = \left(\frac{i \times i_{\text{lim}}}{i_{\text{lim}} - i} \right) \quad (4)$$

By extracting the difference in kinetic current Δi_k at 0.8 V vs. RHE, the mean TOF (turnover frequency) of different samples can be obtained via:

$$\text{TOF}@0.8 \text{ V vs. RHE}(\text{s}^{-1}) = \frac{\Delta i_k (\text{Ag}^{-1})}{F(\text{Asmol}^{-1}) \times \text{MSD(mol g}^{-1}\text{)}} \quad (5)$$

ECSA test followed a published method, being properly estimated from the electrochemical double-layer capacitance of the catalytic surface [42].

The membrane electrode assembly (MEA) preparation and PEMFC test were similar to our previous report [22]. Briefly, the catalyst and Nafion ionomer (weight ratio of 1/1) were mixed in isopropanol/water (volume ratio of 1/1) to form a uniform catalyst ink by sonication and stirring. Afterwards, the homogeneous ink was brushed onto a piece of 5 cm^2 carbon paper (gas diffusion layer, GDL) and dried at 80°C for 2 h under vacuum. The cathode catalyst loading was 3 mg cm^{-2} for NPMC catalysts or $0.5 \text{ mg}_{\text{Pt}} \text{ cm}^{-2}$ for Pt/C(20%) for reference. Anode was Pt/C(20%) with catalyst loading of $0.5 \text{ mg}_{\text{Pt}} \text{ cm}^{-2}$.

A couple of anode and cathode were hot-pressed onto a piece of Nafion 211 membrane (DuPont[®]) at 130°C for 2 min under 300 pounds cm^{-2} pressure to obtain the MEA. Finally, the PEM fuel cell test was performed on a fuel cell test station (Scribner 850e) with UHP

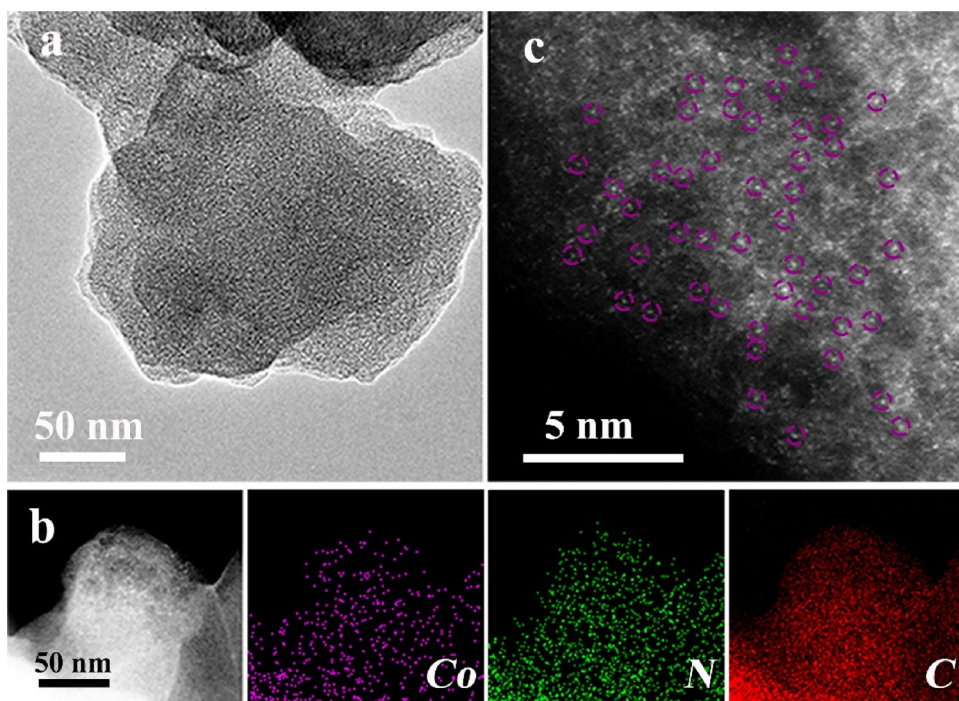


Fig. 1. Morphology and element distribution of 1.6%CoNC-ArNH₃. (a) TEM image, (b) elemental mapping and (c) HAADF-STEM image with circle around individual Co atom.

grade H₂ and O₂ (or air). The gas and cell temperatures were 80 °C. The flow rate of 100% humidified H₂ and O₂ (or air) was 300 and 400 mL min⁻¹, respectively.

2.3. Characterizations

The catalyst morphology was investigated by scanning electron microscopy (SEM, JSM-7500 F, JEOL) and transmission electron microscopy (TEM, JEM-2100 F, JEOL) equipped with an energy-dispersive X-ray spectroscope (EDS, X-Max-65 T, Oxford) for collecting the elemental mapping of the catalysts. The high-angle annular dark field aberration-corrected scanning transmission electron microscopy (HAADF-STEM) was carried out on JEM-ARM200 F at an operating voltage of 200 kV to obtain the atomic resolution image. X-ray diffraction (XRD) was performed on Rigaku D/max 2500PC with Cu K α radiation ($\lambda = 1.54 \text{ \AA}$, 40 kV, 150 mA). X-ray photoelectron spectroscopy (XPS) was performed on an ESCALAB 250 Xi with an Al K α excitation source. Brunauer-Emmett-Teller (BET) surface area and pore-size distribution of the samples were measured with SSA-7000 (Beijing bjbuilder) at 77 K. The samples were degassed under 300 °C overnight before tests.

XAS measurement and data analysis: XAS spectra at the Co K-edge (7709 eV) were measured at the beamline 1W1B station of the Beijing Synchrotron Radiation Facility, China. The Co K-edge X-ray absorption near edge structure (XANES) data were recorded in a fluorescence mode. The storage ring was working at the energy of 2.5 GeV with an average electron current of 250 mA. The acquired extended X-ray absorption fine structure (EXAFS) data were extracted and processed according to the standard procedures using the ATHENA module implemented in the IFEFFIT software packages. The k^3 -weighted EXAFS spectra were obtained by subtracting the post-edge.

2.4. DFT calculations

Density functional theory (DFT) calculations were performed within the generalized gradient approximation (GGA) designed by Perdew-Burke-Ernzerhof (PBE), as implemented in the Vienna ab initio

simulation package (VASP). The projector augmented wave (PAW) method was used to describe the ionic potentials. The plane wave basis set had a high cut off energy of 500 eV throughout the computations. The K -point sampling of the Brillouin zone was obtained using a $1 \times 1 \times 1$ grid generating meshes with their origin centered at the gamma (Γ) point. All calculations were spin polarized and were done until the force of the system converges to 0.01 eV Å⁻¹.

The Gibbs free energy change (ΔG) of intermediates is calculated by

$$\Delta G = \Delta E + \Delta ZPE - T\Delta S \quad (6)$$

ΔE is the energy change obtained from DFT calculations, ΔZPE is the change in zero-point energies, T is the temperature (298.15 K), and ΔS is the change in entropy. The ZPE and entropies of ORR intermediates were calculated from the vibrational frequencies, and the ZPE and entropies of gas-phase molecules were obtained from the standard thermodynamic database. Details of free-energy calculations and DFT energies, ZPE, entropies of ORR intermediates, and molecules are shown in Table S1.

3. Results and discussion

The Co-N-C catalysts were prepared by ball milling a mixture of cobalt acetate (CoAc), 1, 10-phenanthroline and zeolitic imidazolate framework (ZIF-8) at a proper ratio, followed by a pyrolysis in argon at 1000 °C and then in ammonia at 800 °C. The detailed synthesis is described in the experimental section. The catalyst is named as “x%CoNC-ArNH₃” where “x%” indicates the weight percent of CoAc in the precursor mixture. The optimal composition in our catalyst system was electrochemically determined to be 1.6%CoNC-ArNH₃, which has a submicron particle size, a BET surface area of 802 m² g⁻¹ and a micropore dominant porosity (Figs. S1, S2). TEM images in Fig. 1a, S1 and XRD pattern in Fig. S3 show an amorphous carbon substrate without visible Co NPs in the catalyst. The elemental mapping suggests the evenly distributed Co and N elements on the carbon support (Fig. 1b). The HAADF-STEM imaging further shows the atomically distributed Co on carbon substrate (Fig. 1c) without any Co agglomerates.

The local structure of Co atoms in 1.6%CoNC-ArNH₃ was

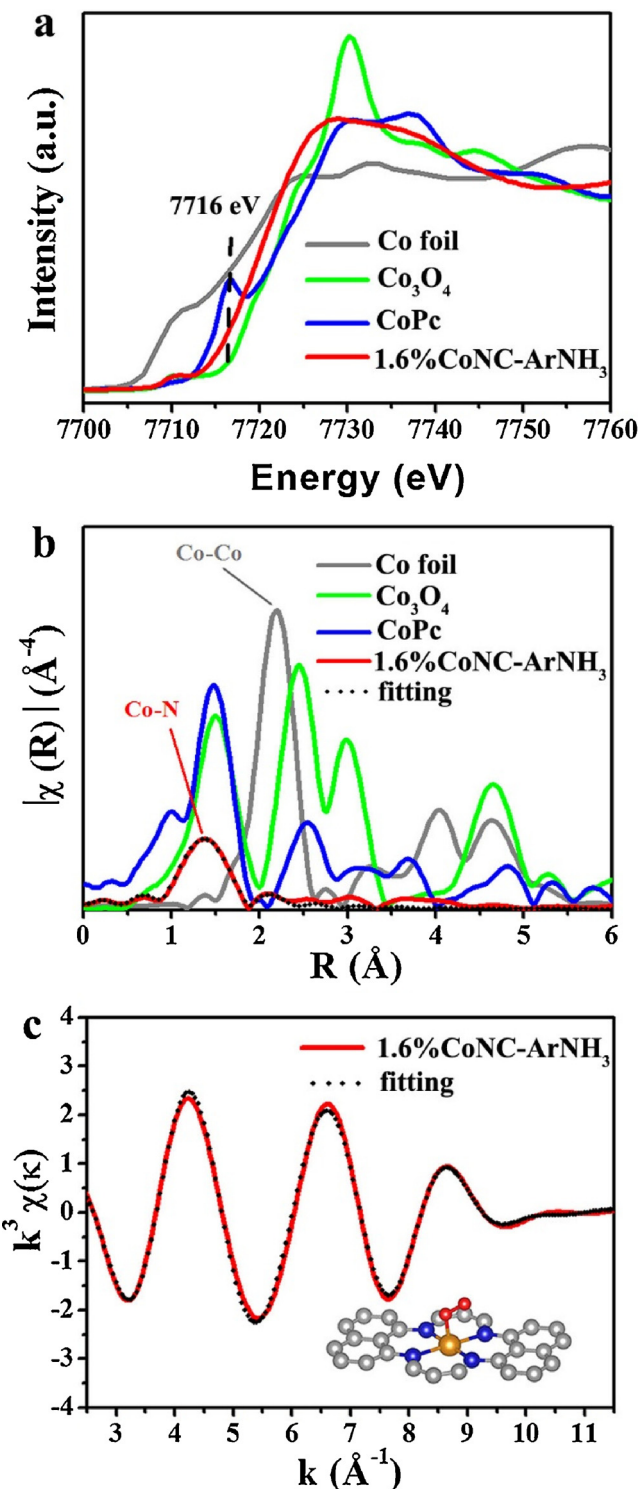


Fig. 2. XANES and EXAFS results of 1.6%CoNC-ArNH₃. (a) The normalized XANES spectra at the Co K-edge and (b) fourier transformed EXAFS (FT-EXAFS) spectra of indicated samples and the R -space fitting for FT-EXAFS of 1.6%CoNC-ArNH₃. (c) The k -space fitting of Co K-edge EXAFS spectrum of 1.6%CoNC-ArNH₃. Inset: Schematic model of CoN₄ moiety in the catalyst. Co (golden), O (red), N (blue) and C (gray) (For interpretation of the references to colour in this figure legend, the reader is referred to the web version of this article).

investigated by XANES and EXAFS measurements at Co K-edge. As shown in Fig. 2a, a pre-edge peak of 1.6%CoNC-ArNH₃ appears around 7711 eV, lower than the pre-edge peak (7716 eV) of cobalt phthalocyanine (CoPc), indicating a certain deviation from the perfect Co-N₄

square planarity and the presence of axial ligand(s) in the active site [43]. The inflection point of 1.6%CoNC-ArNH₃ at 7730 eV is close to that of Co₃O₄, suggesting that the Co valence state is between +2 and +3 [38,43]. The Fourier-transformed (FT) EXAFS spectrum in Fig. 2b shows a strong peak at 1.4 Å, corresponding to the Co-N (or Co-O) coordination. The absence of Co-Co coordination further excludes the metallic Co NPs and confirms the atomic distribution of Co in 1.6%CoNC-ArNH₃. To further analyze the coordination structure around Co atom, the FT-EXAFS data of 1.6%CoNC-ArNH₃ was fitted in R - and k -spaces in Fig. 2b and c. The fitting curves based on the inserted moiety model are in good agreement with the experimental ones. According to the fitting results summarized in Table S2, the Co atom in our catalyst is likely coordinated by four N atoms (i.e. CoN₄) with one end-on adsorbed O₂ molecule that is similar to other literature reports [12,34,37].

1.6%CoNC-ArNH₃ was also analyzed by XPS (Fig. S4). The N and Co contents are determined to be 5.66 and 3.03 wt%, respectively. The Co 2p XPS spectrum can be deconvoluted into three components i.e. Co (III), Co(II) and shake-up peaks, suggesting that the Co valence state is between +2 and +3 consistent with the EXAFS result. The N 1s spectrum is deconvoluted into pyridinic (398.3 eV), pyrrolic (400.3 eV), graphitic-like (401.3 eV) and oxidized (402.4 eV) nitrogen species with contents of 23.6%, 15.8%, 16.4% and 23.9%, respectively [44]. Moreover, another nitrogen species at 399.3 eV with content of 20.3% can be attributed to the pyridinic N bound to Co (Co-N_x) which upshifts 1 eV from pristine pyridinic N [44].

The ORR activity of $x\%$ CoNC-ArNH₃ (x from 0.4 to 1.6) was investigated in O₂ saturated 0.5 M H₂SO₄ by a rotating ring disk electrode (RRDE) measurement (Fig. S5a). We observed an increment of ORR activity with the increase of Co content in the catalysts. The LSV curve of 1.6%CoNC-ArNH₃ (Fig. 3a) presents a good ORR activity with an onset potential (E_{onset}) of 0.89 V and a half-wave potential ($E_{1/2}$) of 0.785 V (vs. RHE). In addition, 1.6%CoNC-ArNH₃ also exhibits a long-term stability (Fig. S5b, c) and a methanol tolerance (Fig. S6). Since the Co atom can be poisoned by SCN⁻ due to the strong affinity between the two species, KSCN was used to identify the role of Co atoms in the catalysis. Once a small amount of KSCN is added into electrolyte, the ORR current of 1.6%CoNC-ArNH₃ decreases significantly, demonstrating that its high ORR activity originates from the atomic CoN₄ sites (Fig. S7).

During ORR process, 1.6%CoNC-ArNH₃ yields 3~10% H₂O₂ suggesting a predominant 4e⁻ pathway (Fig. 3b) [45]. The 4e⁻ ORR can proceed through a direct 4e⁻ pathway or a 2e⁻+2e⁻ pathway [40]. Since the 2e⁻+2e⁻ pathway produces harmful intermediates like H₂O₂ and oxygen radicals, the direct 4e⁻ pathway is more favorable for PEMFC application. In order to distinguish the 2e⁻+2e⁻ pathway and the direct 4e⁻ pathway, we carried out an experimental measurement of peroxide reduction reaction (PRR) on our catalyst in an Ar-saturated electrolyte containing H₂O₂ [40]. The lower PRR activity of 1.6%CoNC-ArNH₃ than those of Pt/C(20%) and Fe-N-C demonstrates that the ORR on 1.6%CoNC-ArNH₃ predominantly occurred through the direct 4e⁻ pathway (Fig. 3b inset and Fig. S8). Li et al. theoretically proposed the direct 4e⁻ pathway for ORR on their Co-N₄ model by DFT calculation [46]. In order to keep the consistency of active site structure, we also performed DFT calculation on our own CoN₄C₁₆ moiety to analyze the ORR process in Fig. S9 (parameters see Table S2). The calculation results support the above PRR experimental observation, proving the direct 4e⁻ ORR on our Co-N-C catalyst.

After half-cell tests, Fig. 4a compares the polarization curves and power density curves of 1.6%CoNC-ArNH₃, Fe-N-C and Pt/C(20%) in a PEMFC device measured with 2.5 bar H₂/O₂. An open-circuit voltage (OCV) of 0.916 V and a current density of 1.8 A cm⁻² at 0.4 V are recorded for 1.6%CoNC-ArNH₃. Its peak power density ranges from 755 to 826 mW cm⁻² with an average value approximately 800 mW cm⁻² (see Fig. S10 for repeating experiments). The achieved high power density is among the top PEMFC performances of Co-N-C catalysts as

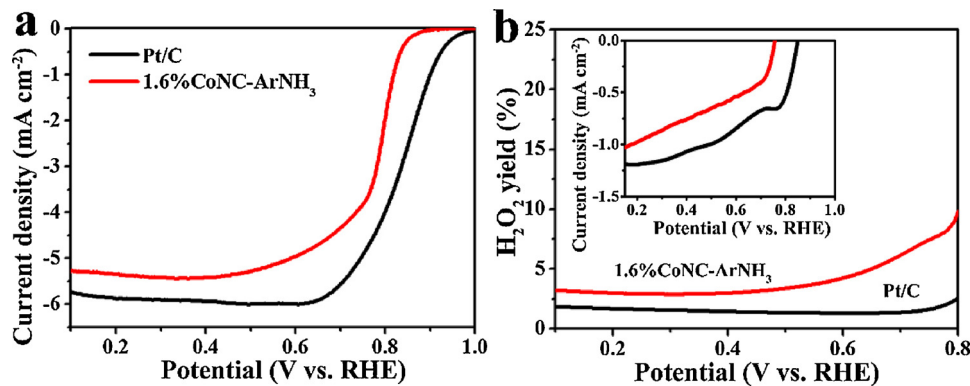


Fig. 3. (a) Linear sweep voltammetry (LSV) curves and (b) corresponding hydrogen peroxide yields of 1.6%CoNC-ArNH₃ (in O₂ saturated 0.5 M H₂SO₄) and Pt/C(20%) (in O₂ saturated 0.1 M HClO₄). The inset in B is PRR polarization curves in Ar saturated 0.1 M HClO₄.

shown in Table S3. Under a relatively low pressure of 1 bar H₂-O₂, the 1.6%CoNC-ArNH₃ can still deliver a remarkable power density of 440 mW cm⁻² (or 502 mW cm⁻² at iR-compensated condition), close to the performance of Fe-N-C as shown in Fig. S11. In our experiment, the high active site density was proved to be the most crucial reason for the excellent PEMFC performance of 1.6%CoNC-ArNH₃, by comparing with other seven samples of x%CoNC-ArNH₃ ($x = 0.4, 0.6, 0.8, 1.0, 1.2, 1.4, 1.8$). The samples 0.4%CoNC-ArNH₃ to 1.6%CoNC-ArNH₃ represent the Co-N-C SACs with increasing CoN₄ moiety density, while 1.8%CoNC-ArNH₃ denotes an over-doped catalyst with Co NPs (Fig. S12). The original polarization and power density curves of the seven control samples are given in Fig. S13.

The active site densities of the above Co-N-C catalysts were measured by an electrochemical methodology reported by Kucernak et al., i.e. a nitrite adsorption first, followed by a reductive stripping in acidic electrolyte [16]. The excess coulombic charge of the stripping peak is proportional to the number of active CoN₄ sites (Fig. S14). The gravimetric active site densities (MSDs) is defined as the amount of active (electrochemically accessible) CoN₄ sites being normalized to the mass of the Co-N-C catalyst. CoN₄ MSDs of 0.4%CoNC-ArNH₃, 0.6%CoNC-

ArNH₃, 0.8%CoNC-ArNH₃, 1.0%CoNC-ArNH₃, 1.2%CoNC-ArNH₃, 1.4%CoNC-ArNH₃ and 1.6%CoNC-ArNH₃ were calculated to be 18.9, 22.8, 26.9, 30.3, 33.0, 35.3 and 39.0 $\mu\text{mol}_{\text{site}} \text{g}^{-1}$ respectively, as shown in Fig. 4b.

We firstly associated the fuel cell power density with the CoN₄ MSD of x%CoNC-ArNH₃ in Fig. 4c. The PEMFC power density displays a proportional relationship with the MSD at the voltages of 0.5, 0.6 and 0.7 V. With the increase of CoN₄ MSD, the fuel cell power densities present slow and linear increment in low concentration region (18.9–30.3 $\mu\text{mol}_{\text{site}} \text{g}^{-1}$), followed by an accelerating trend in high concentration region (above 30.3 $\mu\text{mol}_{\text{site}} \text{g}^{-1}$). The Co aggregation in the sample 1.8%CoNC-ArNH₃ reduced MSD to 35.5 $\mu\text{mol}_{\text{site}} \text{g}^{-1}$, which also caused the large drops of PEMFC power densities. It is thus deduced that the CoN₄ active site density, especially the high-density value, has a significant impact on Co-N-C PEMFC power performance. To exclude the interference of the difference of catalyst layers to the fuel cell performances, we observed the cross-section images of all x %CoNC-ArNH₃ catalyst layers, which have similar thicknesses around 43–44 μm (Fig. S15) and similar porosity (Fig. S16). The similar structure of catalyst layer is indispensable to the accurate quantitative

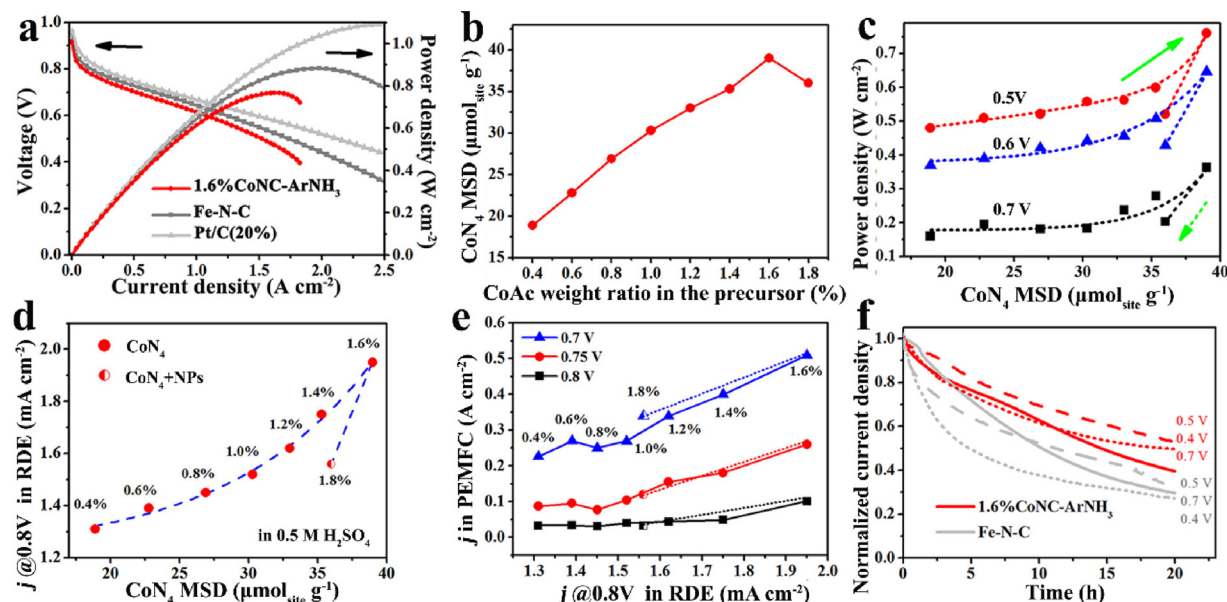


Fig. 4. PEMFC measurements of x%CoNC-ArNH₃ ($x = 0.4 \sim 1.8$) and quantitative analysis. (a) PEMFC polarization and power density curves of the indicated cathode catalysts. (b) The plot of CoN₄ MSD of the catalysts x%CoNC-ArNH₃ as a function of CoAc addition in the precursors. (c) The correlation between CoN₄ MSD and PEMFC power density at the indicated voltages. (d) The plot of ORR activity, i.e. current density j at 0.8 V measured by RDE, as a function of CoN₄ MSD. (e) The correlation between ORR activity and PEMFC current density at 0.7, 0.75 and 0.8 V. (f) Current stability of 1.6%CoNC-ArNH₃ and Fe-N-C catalysts at PEMFC voltages of 0.4 V (dot), 0.5 V (dash) and 0.7 V (solid). Cathode catalyst loading 3 mg cm⁻² for NPMC catalysts and 0.5 mg_{Pt} cm⁻² for Pt/C(20%), H₂/O₂ back pressure 2 bar, 80 °C, 100% relative humidity (RH), Nafion 211 membrane.

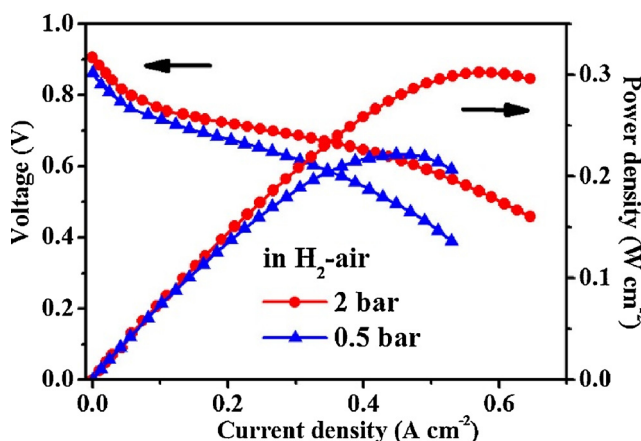


Fig. 5. PEMFC polarization and power density curves of 1.6%CoNC-ArNH₃ measured with H₂-air. (Nafion 211, 80 °C, 100% RH, back pressure 2 and 0.5 bar).

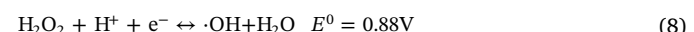
analysis of the relationship between CoN₄ MSD and PEMFC performance.

Fig. 4d shows the plot of ORR activity (current density j at 0.8 V vs. RHE) measured by RDE as a function of CoN₄ MSD. A slightly accelerated increment of ORR activity with the CoN₄ MSD was observed, indicating the importance of high concentration of active sites to the ORR activity of Co-N-C catalysts. Fig. 4e further shows the correlation between ORR activity of x%CoNC-ArNH₃ and their PEMFC current densities at 0.7, 0.75 and 0.8 V. The fuel cell current densities at these voltages present almost linear increase with the ORR activity of the catalyst. It indicates that the performance of Co-N-C fuel cells at the high voltage region (> 0.7 V) is mainly determined by the kinetic activity of the catalyst. The related current densities are summarized in Table S4. In our experiments, the CoN₄ MSD could only reach 39.0 $\mu\text{mol}_{\text{site}} \text{g}^{-1}$. Advanced synthetic methods are the future research direction for Co-N-C SACs which may possess higher active site density and higher fuel cell performance. Since electrocatalysis is a surface process, we also calculated the active site density per electrochemical surface area (ECSA), estimated from the electrochemical double-layer capacitance of the catalyst (Figs. S17, S18) [42]. The ECSA active site densities are approximately 0.69~1.70 ($\times 10^{-6}$) $\mu\text{mol cm}^{-2}$ as summarized in Table S5. The ECSA active site density of 1.70×10^{-6} $\mu\text{mol cm}^{-2}$ for 1.6%CoNC-ArNH₃ equals to 0.90 site nm^{-2} . In other words, there is approximately one CoN₄ active site in one square nanometer of electrolyte accessible catalyst surface.

Based on the CoN₄ quantity and ORR activity in O₂-saturated 0.5 M acetate buffer electrolyte, the mean TOF was calculated to be $\sim 0.01 \text{ s}^{-1}$ at 0.8 V (vs. RHE) for these Co-N-C SACs (Figs. S14 and S19, Table S6). To the best of our knowledge, it is the first report of ORR TOF of CoN₄ active site in acidic media. Although this value is nearly two orders of magnitudes lower than that of FeN_x [16], it is surprising to find that the low TOF of CoN₄ does not significantly restrict the Co-N-C fuel cell power density. This is because the low TOF measured in the half-cell at 0.8 V mainly reflects the sluggish kinetic activity of Co-N-C that dominates the fuel cell polarization loss at the high voltage region. Whereas the high power density appears in the middle voltage range (0.5~0.4 V), where the polarization curve is determined by the combined effects of mass-transport loss, internal resistance loss and kinetic loss. The sluggish ORR kinetics of CoN₄ only influences a part of polarization loss in the high power density region. Hence, despite the relatively low TOF, Co-N-C electrocatalyst is still able to deliver a significant power density as long as it possesses dense CoN₄ active sites. This finding encourages us to explore many neglected NPMCs other than the classic highly active Fe-N-C catalysts for PEMFC application.

The advantage of Co-N-C over Fe-N-C is the higher fuel cell stability.

Fig. 4f shows the normalized current decay of 1.6%CoNC-ArNH₃ at constant voltages of 0.7, 0.5 and 0.4 V with H₂/O₂ feeds. Compared to Fe-N-C with only 35~25% current left after the initial 20 hs aging test, 1.6%CoNC-ArNH₃ maintains 55~40% current, exhibiting more stable performance in the practical voltage range in H₂/O₂ PEMFCs (the original data see Fig. S20). We observed that the fuel cell stability at 0.5 V is better than those at 0.4 and 0.7 V. It may be related to the degree of oxidation and flooding in the cathode catalyst layer, which are determined by the fuel cell voltage. The high voltage causes the high oxidation, and the low voltage (high current) leads to large water production (flooding). The reason for the higher stability of Co-N-C over Fe-N-C was thermodynamically analyzed here. The relevant redox potentials (E^0) of Co, Fe, and H₂O₂/OH are given in Eqs. (1–3) [28].



The lower E^0 in Eq. (7) relative to E^0 in Eq. (8) suggests that the formation of radical ($\cdot\text{OH}$) is thermodynamically favorable on Fe²⁺. However, this reaction is prohibited in the case of Co²⁺ due to the relatively higher E^0 value in Eq. (9). These results support the above direct 4e⁻ ORR pathway on CoN₄. Since the radical attack is one of the reasons for PEMFC performance decay of Fe-N-C, the prohibited $\cdot\text{OH}$ radical formation is believed responsible for the relatively high stability of Co-N-C PEMFC [47].

To validate the catalyst for practical PEMFCs [25], 1.6%CoNC-ArNH₃ was also measured under H₂/air condition as shown in Fig. 5. Compared with H₂/O₂ condition, the fuel cell polarization performance is remarkably reduced due to the oxygen concentration polarization of air. Nevertheless, 1.6%CoNC-ArNH₃ still displays considerable peak power densities of 305 and 221 mW cm⁻² under 2 and 0.5 bar air back pressures, respectively. As expected, 1.6%CoNC-ArNH₃ exhibits a good stability in H₂-air PEMFC at the constant voltage of 0.5 V, as shown in Fig. S21.

4. Conclusions

In summary, a relationship of CoN₄ active site density – PEMFC power density was established based on a series of Co-N-C SACs. The high density of CoN₄ active sites was proved crucial to boost the high PEMFC power density. The 1.6%CoNC-ArNH₃ with the maximum active site density in this work achieved a high power density of 826 mW cm⁻², which is among the top performances of Co-N-C catalysts. Moreover, the ORR TOF of CoN₄ active site was calculated, for the first time to the best of our knowledge, to be approximately 0.01 s⁻¹ at 0.8 V (vs. RHE) in acidic media. In addition, experiments together with theoretical calculations explain the reason for the higher stability of Co-N-C over Fe-N-C. The excellent comprehensive performances of Co-N-C catalyst indicate its promising future for low cost PEMFCs. The disclosed performance enhancement mechanism demonstrates a viable approach to increase the PEMFC power density of non-precious metal catalysts.

Acknowledgement

This work was supported by the National Natural Science Foundation of China (Grant No. 21673014), the Fundamental Research Funds for the Central Universities of China and the 111 project (B17002) funded by the Ministry of Education of China.

Appendix A. Supplementary material

The following information in a PDF file is available free of charge. Supplemental experimental procedures, 21 figures and 6 tables for the

characterizations of the catalysts and performance comparisons.

Appendix B. Supplementary data

Supplementary material related to this article can be found, in the online version, at doi:<https://doi.org/10.1016/j.apcatb.2019.117849>.

References

- [1] P. Atanassov, Fuel Cells: a call for total design, Joule 2 (2018) 1210–1211, <https://doi.org/10.1016/j.joule.2018.03.022>.
- [2] M.K. Debe, Electrocatalyst approaches and challenges for automotive fuel cells, Nature 486 (2012) 43–51, <https://doi.org/10.1038/nature11115>.
- [3] Z.W. Seh, J. Kibsgaard, C.F. Dickens, I. Chorkendorff, J.K. Norskov, T.F. Jaramillo, Combining theory and experiment in electrocatalysis: insights into materials design, Science 355 (2017), <https://doi.org/10.1126/science.aad4998> eaad4998.
- [4] J. Wu, H. Yang, Platinum-based oxygen reduction electrocatalysts, Acc. Chem. Res. 46 (2013) 1848–1857, <https://doi.org/10.1021/ar300359w>.
- [5] J. Liu, M. Jiao, L. Lu, H.M. Barkholtz, Y. Li, Y. Wang, L. Jiang, Z. Wu, D.J. Liu, L. Zhuang, C. Ma, J. Zeng, B. Zhang, D. Su, P. Song, W. Xing, W. Xu, Y. Wang, Z. Jiang, G. Sun, High performance platinum single atom electrocatalyst for oxygen reduction reaction, Nat. Commun. 8 (2017) 15938, <https://doi.org/10.1038/ncomms15938>.
- [6] M. Shao, Q. Chang, J.-P. Dodelet, R. Chenitz, Recent advances in electrocatalysts for oxygen reduction reaction, Chem. Rev. 116 (2016) 3594–3657, <https://doi.org/10.1002/9783527803873.ch20>.
- [7] S. Starika, K. Artyushkova, M.J. Workman, A. Serov, S. McKinney, B. Halevi, P. Atanassov, PGM-free Fe-N-C catalysts for oxygen reduction reaction: catalyst layer design, J. Power Sources 326 (2016) 43–49, <https://doi.org/10.1016/j.jpowsour.2016.06.098>.
- [8] D. He, H. Tang, Z. Kou, M. Pan, X. Sun, J. Zhang, S. Mu, Engineered graphene materials: synthesis and applications for polymer electrolyte membrane fuel cells, Adv. Mater. 29 (2017) 1601741, , <https://doi.org/10.1002/adma.201601741>.
- [9] J. Wang, M. Xu, J. Zhao, H. Fang, Q. Huang, W. Xiao, T. Li, D. Wang, Anchoring ultrafine Pt electrocatalysts on TiO₂-C via photochemical strategy to enhance the stability and efficiency for oxygen reduction reaction, Appl. Catal. B Environ. 237 (2018) 228–236, <https://doi.org/10.1016/j.apcatb.2018.05.085>.
- [10] M. Lefèvre, E. Proietti, F. Jaouen, J.-P. Dodelet, Iron-based catalysts with improved oxygen reduction activity in polymer electrolyte fuel cells, Science 324 (2009) 71–74, <https://doi.org/10.1126/science.1170051>.
- [11] A. Zitolo, V. Goellner, V. Armel, M.T. Sougrati, T. Mineva, L. Stievano, E. Fonda, F. Jaouen, Identification of catalytic sites for oxygen reduction in iron- and nitrogen-doped graphene materials, Nat. Mater. 14 (2015) 937–942, <https://doi.org/10.1038/s41467-017-01100-7>.
- [12] A. Zitolo, N. Ranjbar-Sahraie, T. Mineva, J. Li, Q. Jia, S. Stamatin, G.F. Harrington, S.M. Lyth, P. Krtík, S. Mukerjee, E. Fonda, F. Jaouen, Identification of catalytic sites in cobalt-nitrogen-carbon materials for the oxygen reduction reaction, Nat. Commun. 8 (2017) 957, <https://doi.org/10.1038/s41467-017-01100-7>.
- [13] X. Wan, X. Liu, Y. Li, R. Yu, L. Zheng, W. Yan, H. Wang, M. Xu, J. Shui, Fe-N-C electrocatalyst with dense active sites and efficient mass transport for high-performance proton exchange membrane fuel cells, Nat. Catal. 2 (2019) 259–268, <https://doi.org/10.1038/s41929-019-0237-3>.
- [14] S. Cai, Z. Meng, H. Tang, Y. Wang, P. Tsikaras, 3D Co-N-doped hollow carbon spheres as excellent bifunctional electrocatalysts for oxygen reduction reaction and oxygen evolution reaction, Appl. Catal. B Environ. 217 (2017) 477–484, <https://doi.org/10.1016/j.apcatb.2017.06.008>.
- [15] X. Wan, W. Chen, J. Yang, M. Liu, X. Liu, J. Shui, Synthesis and active site identification of Fe-N-C single-atom catalysts for oxygen reduction reaction, ChemElectroChem 6 (2018) 304–315, <https://doi.org/10.1002/celc.201801302>.
- [16] D. Malko, A. Kucernak, T. Lopes, In situ electrochemical quantification of active sites in Fe-N/C non-precious metal catalysts, Nat. Commun. 7 (2016) 13285, <https://doi.org/10.1038/ncomms13285>.
- [17] Z. Geng, Y. Cao, W. Chen, X. Kong, Y. Liu, T. Yao, Y. Lin, Regulating the coordination environment of Co single atoms for achieving efficient electrocatalytic activity in CO₂ reduction, Appl. Catal. B Environ. 240 (2019) 234–240, <https://doi.org/10.1016/j.apcatb.2018.08.075>.
- [18] Y. Mun, M.J. Kim, S.-A. Park, E. Lee, Y. Ye, S. Lee, Y.-T. Kim, S. Kim, O.-H. Kim, Y.-H. Cho, Y.-E. Sung, J. Lee, Soft-template synthesis of mesoporous non-precious metal catalyst with Fe-Nx/C active sites for oxygen reduction reaction in fuel cells, Appl. Catal. B Environ. 222 (2018) 191–199, <https://doi.org/10.1016/j.apcatb.2017.10.015>.
- [19] W. Wang, W. Chen, P. Miao, J. Luo, Z. Wei, S. Chen, NaCl crystallites as dual-functional and water-removable templates to synthesize a three-dimensional graphene-like macroporous Fe-N-C catalyst, ACS Catal. 7 (2017) 6144–6149, <https://doi.org/10.1021/acscatal.7b01695>.
- [20] E. Proietti, F. Jaouen, M. Lefèvre, N. Larouche, J. Tian, J. Herranz, J.P. Dodelet, Iron-based cathode catalyst with enhanced power density in polymer electrolyte membrane fuel cells, Nat. Commun. 2 (2011) 416, <https://doi.org/10.1038/ncomms1427>.
- [21] G. Wu, K.L. More, C.M. Johnston, P. Zelenay, High-performance electrocatalysts for oxygen reduction derived from polyaniline, iron, and cobalt, Science 332 (2011) 443–447, <https://doi.org/10.1126/science.1200832>.
- [22] J. Shui, C. Chen, L. Grabstanowicz, D. Zhao, D.-J. Liu, Highly efficient nonprecious metal catalyst prepared with metal-organic framework in a continuous carbon nanofibrous network, Proc. Natl. Acad. Sci. U. S. A. 112 (2015) 10629–10634, <https://doi.org/10.1073/pnas.1507159112>.
- [23] Q. Liu, X. Liu, L. Zheng, J. Shui, The solid-phase synthesis of an Fe-N-C electrocatalyst for high-power proton-exchange membrane fuel cells, Angew. Chem. Int. Ed. 57 (2018) 1204–1208, <https://doi.org/10.1002/anie.201709597>.
- [24] X. Fu, P. Zamani, J.Y. Choi, F.M. Hassan, G. Jiang, D.C. Higgins, Y. Zhang, M.A. Hoque, Z. Chen, In situ polymer graphenization ingrained with nanoporosity in a nitrogenous electrocatalyst boosting the performance of polymer-electrolyte-membrane fuel cells, Adv. Mater. 29 (2017) 1604456, , <https://doi.org/10.1002/adma.201604456>.
- [25] H.T. Chung, D.A. Cullen, D. Higgins, B.T. Snead, E.F. Holby, K.L. More, P. Zelenay, Direct atomic-level insight into the active sites of a high-performance PGM-free ORR catalyst, Science 357 (2017) 479–484, <https://doi.org/10.1126/science.aan2255>.
- [26] C. Zhang, Y.C. Wang, B. An, R. Huang, C. Wang, Z. Zhou, W. Lin, Networking pyrolyzed zeolitic imidazolate frameworks by carbon nanotubes improves conductivity and enhances oxygen-reduction performance in polymer-electrolyte-membrane fuel cells, Adv. Mater. 29 (2017) 1604556, , <https://doi.org/10.1002/adma.201604556>.
- [27] L. Yang, D. Cheng, H. Xu, X. Zeng, X. Wan, J. Shui, Z. Xiang, D. Cao, Unveiling the high-activity origin of single-atom iron catalysts for oxygen reduction reaction, Proc. Natl. Acad. Sci. U. S. A. 115 (2018) 6626–6631, <https://doi.org/10.1073/pnas.1800771115>.
- [28] D. Banham, S. Ye, K. Pei, J.-i. Ozaki, T. Kishimoto, Y. Imashiro, A review of the stability and durability of non-precious metal catalysts for the oxygen reduction reaction in proton exchange membrane fuel cells, J. Power Sources 285 (2015) 334–348, <https://doi.org/10.1016/j.jpowsour.2015.03.047>.
- [29] R. Chenitz, U.I. Kramm, M. Lefèvre, V. Glibin, G. Zhang, S. Sun, J.-P. Dodelet, A specific demetalation of Fe-N₄ catalytic sites in the micropores of NC_xAr + NH₃ is at the origin of the initial activity loss of the highly active Fe/N/C catalyst used for the reduction of oxygen in PEM fuel cells, Energy Environ. Sci. 11 (2018) 365–382, <https://doi.org/10.1039/C7EE02302B>.
- [30] X. Zeng, J. Shui, X. Liu, Q. Liu, Y. Li, J. Shang, L. Zheng, R. Yu, Single-atom to single-atom grafting of Pt₁ onto Fe-N₄ center: Pt₁@Fe-N-C multifunctional electrocatalyst with significantly enhanced properties, Adv. Energy Mater. 8 (2018) 1701345, , <https://doi.org/10.1002/aenm.201701345>.
- [31] J.-Y. Choi, L. Yang, T. Kishimoto, X. Fu, S. Ye, Z. Chen, D. Banham, Is the rapid initial performance loss of Fe/N/C non precious metal catalysts due to micropore flooding? Energy Environ. Sci. 10 (2017) 296–305, <https://doi.org/10.1039/C6EE03005J>.
- [32] C.H. Choi, H.-K. Lim, M.W. Chung, G. Chon, N. Ranjbar Sahraie, A. Altin, M.-T. Sougrati, L. Stievano, H.S. Oh, E.S. Park, F. Luo, P. Strasser, G. Dražić, K.J.J. Mayrhofer, H. Kim, F. Jaouen, The Achilles' heel of iron-based catalysts during oxygen reduction in an acidic medium, Energy Environ. Sci. 11 (2018) 3176–3182, <https://doi.org/10.1039/C8EE01855C>.
- [33] R. Bashyam, P. Zelenay, A class of non-precious metal composite catalysts for fuel cells, Nature 443 (2006) 63–66, <https://doi.org/10.1038/nature05118>.
- [34] X.X. Wang, D.A. Cullen, Y.T. Pan, S. Hwang, M. Wang, Z. Feng, J. Wang, M.H. Engelhard, H. Zhang, Y. He, Y. Shao, D. Su, K.L. More, J.S. Spendelow, G. Wu, Nitrogen-coordinated single cobalt atom catalysts for oxygen reduction in proton exchange membrane fuel cells, Adv. Mater. 30 (2018) 1706758, , <https://doi.org/10.1002/adma.201706758>.
- [35] Q.Q. Cheng, L.J. Yang, L.L. Zou, Z.Q. Zou, C. Chen, Z. Hu, H. Yang, Single cobalt atom and N codoped carbon nanofibers as highly durable electrocatalyst for oxygen reduction reaction, ACS Catal. 7 (2017) 6864–6871, <https://doi.org/10.1021/acscatal.7b02326>.
- [36] Y. He, S. Hwang, D.A. Cullen, M.A. Uddin, L. Langhorst, B. Li, S. Karakalos, A.J. Kropf, E.C. Wegener, J. Sokolowski, M. Chen, D. Myers, D. Su, K.L. More, G. Wang, S. Litster, G. Wu, Highly active atomically dispersed CoN₄ fuel cell cathode catalysts derived from surfactant-assisted MOFs: carbon-shell confinement strategy, Energy Environ. Sci. 12 (2019) 250–260, <https://doi.org/10.1039/C8EE02694G>.
- [37] P.Q. Yin, T. Yao, Y. Wu, L.R. Zheng, Y. Lin, W. Liu, H.X. Ju, J.F. Zhu, X. Hong, Z.X. Deng, G. Zhou, S.Q. Wei, Y.D. Li, Single cobalt atoms with precise N-coordination as superior oxygen reduction reaction catalysts, Angew. Chem. Int. Ed. 55 (2016) 10800–10805, <https://doi.org/10.1002/ange.201604802>.
- [38] Y. Zheng, Y. Jiao, Y. Zhu, Q. Cai, A. Vasileff, L.H. Li, Y. Han, Y. Chen, S.Z. Qiao, Molecule-level g-C₃N₄ coordinated transition metals as a new class of electrocatalysts for oxygen electrode reactions, J. Am. Chem. Soc. 139 (2017) 3336–3339, <https://doi.org/10.1021/jacs.6b13100>.
- [39] Y. Chen, S. Ji, C. Chen, Q. Peng, D. Wang, Y. Li, Single-atom catalysts: synthetic strategies and electrochemical applications, Joule 2 (2018) 1242–1264, <https://doi.org/10.1016/j.joule.2018.06.019>.
- [40] C.H. Choi, W.S. Choi, O. Kasian, A.K. Mechler, M.T. Sougrati, S. Bruller, K. Strickland, Q. Jia, S. Mukerjee, K.J.J. Mayrhofer, F. Jaouen, Unraveling the nature of sites active toward hydrogen peroxide reduction in Fe-N/C catalysts, Angew. Chem. Int. Ed. 56 (2017) 8809–8812, <https://doi.org/10.1002/anie.201704356>.
- [41] D. Malko, A. Kucernak, T. Lopes, Performance of Fe-N/C oxygen reduction electrocatalysts toward NO², NO, and NH₂OH electroreduction: from fundamental insights into the active center to a new method for environmental nitrite destruction, J. Am. Chem. Soc. 138 (2016) 16056–16068, <https://doi.org/10.1021/jacs.6b09622>.
- [42] X. Fu, F.M. Hassan, P. Zamani, G. Jiang, D.C. Higgins, J.-Y. Choi, X. Wang, P. Xu, Y. Liu, Z. Chen, Engineered architecture of nitrogenous graphene encapsulating

- orous carbon with nano-channel reactors enhancing the PEM fuel cell performance, *Nano Energy* 42 (2017) 249–256, <https://doi.org/10.1016/j.nanoen.2017.10.051>.
- [43] W. Liu, L. Zhang, W. Yan, X. Liu, X. Yang, S. Miao, W. Wang, A. Wang, T. Zhang, Single-atom dispersed Co–N–C catalyst: structure identification and performance for hydrogenative coupling of nitroarenes, *Chem. Sci.* 7 (2016) 5758–5764, <https://doi.org/10.1039/c6sc02105k>.
- [44] C. Tang, B. Wang, H.F. Wang, Q. Zhang, Defect engineering toward atomic Co-N_x-C in hierarchical graphene for rechargeable flexible solid Zn-air batteries, *Adv. Mater.* 29 (2017) 1703185, , <https://doi.org/10.1002/adma.201703185>.
- [45] Y. Han, Y.G. Wang, W. Chen, R. Xu, L. Zheng, J. Zhang, J. Luo, R.A. Shen, Y. Zhu, W.C. Cheong, C. Chen, Q. Peng, D. Wang, Y. Li, Hollow N-doped carbon spheres with isolated cobalt single atomic sites: superior electrocatalysts for oxygen reduction, *J. Am. Chem. Soc.* 139 (2017) 17269–17272, <https://doi.org/10.1021/jacs.7b10194>.
- [46] F. Li, H. Shu, C. Hu, Z. Shi, X. Liu, P. Liang, X. Chen, Atomic mechanism of electrocatalytically active Co-N complexes in graphene basal plane for oxygen reduction reaction, *ACS Appl. Mater. Interfaces* 7 (2015) 27405–27413, <https://doi.org/10.1021/acsami.5b09169>.
- [47] X.X. Wang, V. Prabhakaran, Y. He, Y. Shao, G. Wu, Iron-free cathode catalysts for proton-exchange membrane fuel cells: cobalt catalysts and the peroxide mitigation approach, *Adv. Mater.* (2019) 1805126, , <https://doi.org/10.1002/adma.201805126>.